

## A Conformal, Bio-Interfaced Class of Silicon Electronics for Mapping Cardiac Electrophysiology

Jonathan Viventi, *et al.*

*Sci Transl Med* 2, 24ra22 (2010);

DOI: 10.1126/scitranslmed.3000738

**A complete electronic version of this article** and other services, including high-resolution figures, can be found at:

<http://stm.sciencemag.org/content/2/24/24ra22.full.html>

**Supporting Online Material** can be found at:

"Supplementary Material"

<http://stm.sciencemag.org/content/suppl/2010/03/19/2.24.24ra22.DC1.html>

This article **cites 22 articles**, 9 of which can be accessed free:

<http://stm.sciencemag.org/content/2/24/24ra22.full.html#ref-list-1>

Information about obtaining **reprints** of this article or about obtaining **permission to reproduce this article** in whole or in part can be found at:

<http://www.sciencemag.org/about/permissions.dtl>

## CARDIAC ELECTROPHYSIOLOGY

# A Conformal, Bio-Interfaced Class of Silicon Electronics for Mapping Cardiac Electrophysiology

Jonathan Viventi,<sup>1\*</sup> Dae-Hyeong Kim,<sup>2\*</sup> Joshua D. Moss,<sup>3</sup> Yun-Soung Kim,<sup>2</sup> Justin A. Blanco,<sup>1</sup> Nicholas Annetta,<sup>4</sup> Andrew Hicks,<sup>1</sup> Jianliang Xiao,<sup>5,6</sup> Younggang Huang,<sup>5,6</sup> David J. Callans,<sup>3</sup> John A. Rogers,<sup>2†</sup> Brian Litt<sup>1,7†</sup>

(Published 24 March 2010; Volume 2 Issue 24 24ra22)

In all current implantable medical devices such as pacemakers, deep brain stimulators, and epilepsy treatment devices, each electrode is independently connected to separate control systems. The ability of these devices to sample and stimulate tissues is hindered by this configuration and by the rigid, planar nature of the electronics and the electrode-tissue interfaces. Here, we report the development of a class of mechanically flexible silicon electronics for multiplexed measurement of signals in an intimate, conformal integrated mode on the dynamic, three-dimensional surfaces of soft tissues in the human body. We demonstrate this technology in sensor systems composed of 2016 silicon nanomembrane transistors configured to record electrical activity directly from the curved, wet surface of a beating porcine heart *in vivo*. The devices sample with simultaneous sub-millimeter and submillisecond resolution through 288 amplified and multiplexed channels. We use this system to map the spread of spontaneous and paced ventricular depolarization in real time, at high resolution, on the epicardial surface in a porcine animal model. This demonstration is one example of many possible uses of this technology in minimally invasive medical devices.

## INTRODUCTION

Conventional tools for managing and treating cardiac arrhythmias use sparse arrays of rigid electrodes arranged on a cylindrical catheter that record electrical potentials at the surface of cardiac tissue at one or a few spatial locations at a time. During mapping, these catheters are inserted through the chest wall and maneuvered from place to place from outside the body to record from discrete sites on the heart. In both cases, sequential local recordings are “stitched” together with software to yield a complete representation of cardiac electrical activity over a region of interest. The iterative nature of this approach often requires more than 1 hour in the electrophysiology lab and prevents real-time mapping of transient abnormal rhythms (1, 2). One means to facilitate mapping and ablation is to integrate large numbers of distributed sensors and electronics over the surface of the heart to provide full, spatio-temporal evaluation of cardiac electrical rhythms in real time. At present, however, all forms of high-performance electronics are built on the hard, rigid, and brittle surfaces of semiconductor wafers, in formats that are inherently incompatible with establishing intimate, large area interfaces with the curvilinear surfaces of the body. Newer flexible, stretchable electron-

ics have the potential to avoid these limitations, but existing devices offer only simple modes of functionality, without the necessary levels of integration or performance needed to provide clinically useful operation for real-time spatio-temporal mapping (3–13). These technologies also cannot yet operate when immersed in biological fluids as required for medical use because of extreme difficulties in electrically isolating the devices to prevent leakage currents that can shock the contacting tissue (3–11).

Here, we report a high-performance, conformal electronic system capable of intimate integration with dynamic, living biological tissues. We apply this approach in a sensor system configured to measure cardiac electrophysiological activity with high temporal and spatial resolution, and we validate its performance *in situ* in a porcine animal model.

## RESULTS

### Fabrication

Fabrication begins with doped single crystal silicon nanoribbons on a silicon wafer that are transfer-printed to a thin plastic sheet (Fig. 1, A to D). Deposition and patterning of suitable dielectric and metal layers complete the functional electronics. Specialized designs and multilayer encapsulation schemes protect all active components from the tissue and surrounding biofluids. The completed device appears in Fig. 1E, and fabrication details are included in Materials and Methods and Supplementary Material. The device includes an 18 × 16 array of amplified electrodes to provide a total of 288 measurement points spaced 800- $\mu$ m apart and covering a total area of 14.4 mm by 12.8 mm (Fig. 1). Each electrode consists of a gold contact pad that serves as an electrical interface with the tissue, connected to an associated amplifier and multiplexer. A single amplifier, multi-

<sup>1</sup>Department of Bioengineering, University of Pennsylvania, Philadelphia, PA 19104, USA. <sup>2</sup>Department of Materials Science and Engineering, Beckman Institute for Advanced Science and Technology, and Frederick Seitz Materials Research Laboratory, University of Illinois, Urbana, IL 61801, USA. <sup>3</sup>Division of Cardiology, Department of Medicine, Hospital of the University of Pennsylvania, 9 Founders Pavilion, 3400 Spruce Street, Philadelphia, PA 19104, USA. <sup>4</sup>Department of Electrical and Systems Engineering, University of Pennsylvania, Philadelphia, PA 19104, USA. <sup>5</sup>Department of Mechanical Engineering, Northwestern University, Evanston, IL 60208, USA. <sup>6</sup>Department of Civil and Environmental Engineering, Northwestern University, Evanston, IL 60208, USA. <sup>7</sup>Penn Epilepsy Center, Department of Neurology, Hospital of the University of Pennsylvania, 3 West Gates, 3400 Spruce Street, Philadelphia, PA 19104, USA.

\*These authors contributed equally to this work.

†To whom correspondence should be addressed. E-mail: littb@mail.med.upenn.edu (B.L.); jrogers@uiuc.edu (J.A.R.)

plexer, and electrode make up a unit cell. Each unit cell comprises 7 n-type metal-oxide-semiconductor (nMOS) field-effect transistors for a total of 2016. Integrated multiplexing circuitry enables the use of only 36 wires to connect all 288 measurement points to external data acquisition (DAQ) and control units.

The transistors and interconnections were formed in four layers, as illustrated in Fig. 1 (A to D). In the first step, transfer printing delivers to a flexible plastic substrate [polyimide (PI);  $\sim 25 \mu\text{m}$  thick], an organized collection of single-crystalline, semiconductor-grade silicon nanomembranes (260 nm) with patterned regions of n-type (phosphorus) doping (Fig. 1A). Plasma-enhanced chemical vapor deposition of  $\text{SiO}_2$  ( $\sim 100 \text{ nm}$ ) at a reduced temperature ( $\sim 250^\circ\text{C}$ ) yields a gate dielectric through which source or drain contact openings are formed by photolithography and etching in buffered oxide etchant. Electron beam evaporation, photolithography, and wet etching define the first layer of metal interconnections, including source, drain, and gate contacts (Fig. 1B). Similarly fabricated second and third metal layers form the column and row addressing electrodes (Fig. 1, C and D). A thin layer of spin-cast PI ( $1.4 \mu\text{m}$ ) with etched vertical interconnect access holes provides the interlayer dielectric between the first and the second metal layers; a trilayer organic or inorganic stack (PI/ $\text{Si}_3\text{N}_4$ /epoxy,  $1.4 \mu\text{m}/80 \text{ nm}/9 \mu\text{m}$ ) and a single layer of epoxy ( $9 \mu\text{m}$ ) form a similar interlayer for the second and third and third and fourth metal layers, respectively. The completed device appears in Fig. 1E. Details are outlined in figs. S1 to S5.

## Design

This layered structure locates the circuit at the neutral mechanical plane to prevent damage from bending and to ensure reliable operation when the device is immersed in saline solution and biofluids, as described below. The top metal layer contains the surface electrodes (Au pads,  $250 \times 250 \mu\text{m}$ ) that contact the cardiac tissue and connect to the underlying circuits through vertical interconnect access holes. These electrodes have output impedances of  $100 \text{ kilohm} \pm 10\%$  at  $1 \text{ kHz}$ , as measured with a similarly designed passive electrode array immersed in normal saline (0.9%) solution. (Measuring the output impedance of the metal electrodes is not possible when they are integrated with the active circuitry.) The entire device connects to a DAQ system through an anisotropic conductive film (ACF) connector with 36 contacts. See fig. S6 for more details and for dimensions of the devices.

The right panels of Fig. 1C and Fig. 2A provide annotated images and circuit diagrams, respectively, of the amplifier and the multiplexing transistor. The amplifier uses a source-follower configuration with current gain (fig. S7). The multiplexing transistor enables read-out of all inputs via programmed, sequential addressing of each row of electrodes, thereby providing a 16 times reduction in the required number of output wires relative to a nonmultiplexed electrode array.

The schematic in Fig. 2B illustrates how the unit cell in Fig. 2A connects to other unit cells to create the multiplexed signal output. This basic layout allows the design to be easily scaled up to larger overall array sizes while maintaining the spatial resolution of the array and without adding substantially more wires. During multiplexed sampling, one row of electrodes at a time is selected by driving one of the row select signals, such as  $R_0$  (highlighted in blue in Fig. 2B), high and all of the others low ( $R_1 \dots R_n$ , where  $R_1$  is highlighted in green). This scheme allows the unit cells in the corresponding row to drive the column output lines ( $C_0 \dots C_m$ , where  $C_0$  is

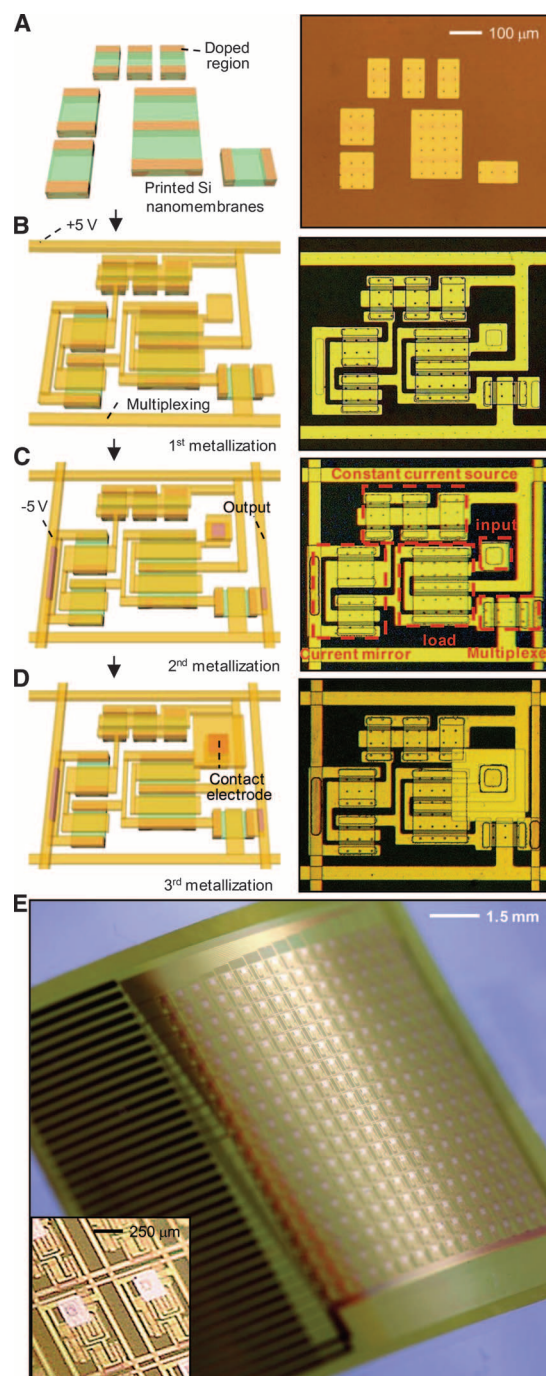


**Fig. 1.** Schematic illustrations and images of steps for fabricating active, conformal electronics for cardiac electrophysiology, and photograph of a completed device. (A) Schematic illustration (left) and optical micrograph (right) of a collection of doped silicon nanomembranes in a unit cell. (B) Configuration after fabrication of the source, drain, and gate contacts, with suitable interconnects and row electrodes for multiplexed addressing. (C) Configuration after fabrication of the second metal layer, including the column output electrodes. Annotations at right indicate the multiplexing transistor and the various components of the amplifier. (D) Final layout after deposition of encapsulation layers and fabrication of the tissue-contacting electrode. (E) Photograph of a completed device in a slightly bent state. (Inset) Magnified view of a pair of unit cells.

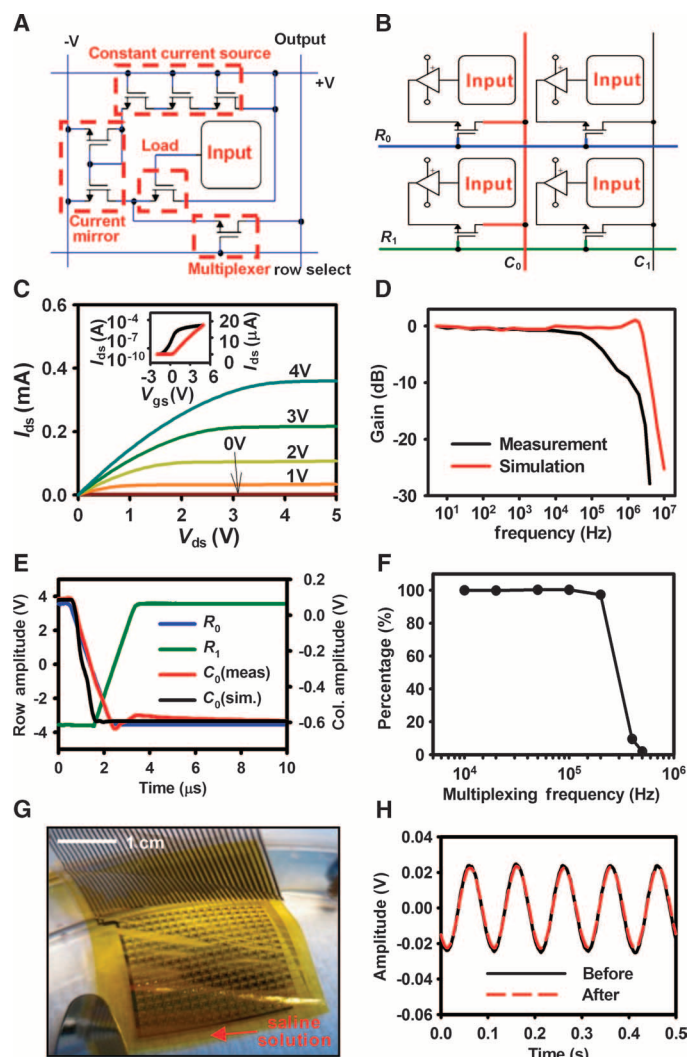


**Fig. 2.** Design and electrical properties of an active, flexible device for cardiac electrophysiological mapping. **(A)** Circuit diagram for a unit cell, with annotations corresponding to those in Fig. 1C. **(B)** Circuit diagram of four unit cells, indicating the scheme for multiplexed addressing. **(C)** Current-voltage characteristics of a representative flexible silicon transistor. Drain to source current ( $I_{ds}$ ) is plotted as a function of drain to source voltages ( $V_{ds}$ ). The gate to source voltage ( $V_{gs}$ ) is varied from 0 to 4 V in 1-V steps. (Inset)  $I_d$  on logarithmic (left) and linear scales (right), as  $V_{gs}$  is swept from  $-2$  to  $+5$  V, demonstrating the threshold voltage ( $V_t$ ) of the transistor. **(D)** Simulated and measured frequency response of a representative amplifier with multiplexing disabled. The amplifier shows performance properties consistent with design targets and simulations (that is,  $-3$  dB cutoff frequency of  $\sim 200$  kHz). Simulations were obtained using commercial software (Cadence, Cadence Design Systems; see the Supplementary Material for simulation details). **(E)** Representative multiplexer switching response, showing the row select signals, column output, and simulated column output. The response time is limited by the external row select signal slew rate. **(F)** Percentage of the final voltage value attained during the allotted settling time, averaged across all of the electrodes, for increasing multiplexing frequency, indicating that the maximum useable multiplexing rate is  $\sim 200$  kHz. **(G)** Photograph of a completed device with ACF interconnect immersed in a saline solution. **(H)** Sine wave response (at 10 Hz) before and after saline immersion for 3 hours.

highlighted in red), which are connected to a high-speed analog to digital converter (fig. S8). Row select signals are rapidly cycled to sample all electrodes on the array.

### Properties

The multiplexing transistors exhibit on-off ratios of  $\sim 10^5$  and electron mobilities of  $\sim 490$   $\text{cm}^2/\text{Vs}$ , calculated from the ratio of maximum and minimum current outputs and the slopes of the transfer curves (inset), respectively, by using standard field-effect transistor models (14) (Fig. 2C). The high mobility of single-crystalline silicon, relative to organics or other materials for flexible electronics, enables the amplifier to have a high bandwidth (Fig. 2D), and the multiplexer to switch quickly (Fig. 2E), even for the relatively coarse dimensions of the devices reported here (channel lengths of  $\sim 40$   $\mu\text{m}$ ). The switching time ( $\sim 5$   $\mu\text{s}$ ) is limited, however, by the slew rate of the external row select signals provided to the array, as shown in blue and green in Fig. 2E. We also determined the percentage of the final voltage value attained during the allotted settling time, averaged across all of the electrodes, with increasing multiplexing frequency (Fig. 2F). Multiplexing rates up to 200 kHz were measured, yielding usable sampling rates up to 12.5 kHz per electrode. The signal-to-noise ratio (SNR) for the system remains constant up to 200 kHz multiplexing frequency (fig. S9). The SNR calculation corresponds to signal to noise and distortion (SINAD) for a 50-mV peak-to-peak sine wave at 20 Hz. The high value for SINAD indicates that there is very little nonlinear distortion introduced by the device. The SNR measurements (fig. S9) and the voltage shifts between adjacent channels (Fig. 2E) indicate that cross talk is negligible for typical signal levels.

In experiments described below, the 16 row select signals were cycled at 10 kHz, yielding a sampling rate of 625 Hz per active electrode, with all 16 electrodes in a given row thus sampled sequentially. The multiplexed analog signals were synchronously sampled at 50 kHz, with five times oversampling per switch interval to improve the SNR. If the slew rate of the row select signals is increased via improvements in the DAQ system, the multiplexing rate can be further increased.

### Mechanical flexibility

We used analytical mechanics modeling to explore the bending-induced strains in all layers of the devices used in our animal experiments. For bending radii of  $\sim 5$  cm, typical of those used in commercially available electrophysiology catheter designs, maximum strains in Si and  $\text{SiO}_2$  are found to be 0.001% and 0.0001%, respectively. These values are three to four orders of magnitude below the fracture strain for Si and  $\text{SiO}_2$  ( $\sim 1\%$ ), and they are also considerably less than those expected to alter their electrical performance (15). The induced strains remain below the fracture limits to radii of curvature as small as 500  $\mu\text{m}$  (fig. S10), thereby enabling, in principle, the array to be rolled into a catheter of only a few millimeters in diameter and unrolled once delivered to the target tissue. Tight folding tests, to radii as small as 500  $\mu\text{m}$ , confirmed that the circuits remain operational under such conditions even after several days.

We also tested whether the bending stiffness of the circuit is sufficiently low to allow conformal wrapping on the moist surface of the cardiac tissue. These mechanics can be modeled by comparing the system energy for a circuit in a flat configuration to one in a wrapped state (fig. S11). The result is that wrapping is energetically favored

when  $\gamma > B / 2R^2$ , where  $\gamma$  is the adhesion energy between the circuit and the tissue,  $R$  is the radius of curvature, and  $B$  is the bending stiffness of the circuit. By using  $R$  of  $\sim 2.5$  cm and a computed value of  $B$ , one finds that wrapping is the preferred configuration for cases where  $\gamma > 34.7$  mJ/m<sup>2</sup>. The reported value of adhesion energy between two wet surfaces is  $\sim 75$  to  $150$  mJ/m<sup>2</sup> (16–18). Our model therefore predicts that the circuits will naturally wrap around the partially wet surface of the cardiac tissue without any separate mechanism to ensure adhesion. This result was validated in our experiments in the porcine model.

### Operation in biological fluids

For use in clinical settings, the circuit must provide sustained operation while immersed in the fluids of the body. We found that our inorganic or organic encapsulation of the circuit serves as an effective water barrier. We immersed the circuit in a saline bath to test for leakage currents from either the positive or the negative power supply by creating a conduction path from the device to a separate ground electrode in the bath (Fig. 2G). Positive and negative power supplies are required to allow the amplifier to remain linear for small positive or negative physiologic signals centered around 0 V.

We selected a cutoff value of  $10 \mu\text{A}$ , consistent with the International Electrotechnical Commission standards for medical electronic equipment (IEC 60601-1). About 75% of the fabricated devices (all electrodes included) passed the leakage current test. Randomly selected samples, typically one from each fabrication batch of four devices, that passed the initial leakage current test were tested for long-term reliability in the saline bath, and most were found to operate for greater than 3 hours while maintaining a leakage current of  $<10 \mu\text{A}$ . Figure 2H shows the device response to a 10-Hz sine wave input before and after saline immersion for 3 hours, verifying that there were negligible changes in circuit properties. Results with a 5-Hz input are also displayed in fig. S12.

### Cardiac monitoring in a porcine model

In vivo experiments were performed in two normal 80- to 90-pound male Yorkshire pigs. The heart was surgically exposed via a median sternotomy and subsequent pericardiotomy. A flexible electrode device was then placed on the epicardial surface under direct visualization (Fig. 3A, fig. S13, and movie M1). The device adhered to the curvilinear surface of the heart, even during the vigorous cardiac motion of rapid pacing. Figure 3B shows motion snapshots at various stages of the cardiac cycle; the blue lines highlight the dynamic variations in the surface shape associated with maintaining conformal contact. Given the average heart rate of  $\sim 77$  beats per minute during in vivo experiments and a recording duration of  $\sim 137$  min, the device provided reliable data over the course of  $>10,000$  bending cycles. Unipolar voltage data were recorded from all 288 electrodes with the sampling and multiplexing strategy described above. Baseline data were collected in sinus rhythm with the array in multiple positions and orientations on the epicardial surface. We also recorded while pacing the heart with a bipolar electrode at multiple locations relative to the array. The distance of the pacing electrode from the array varied from 2 to 5 cm during different experiments. The pacing electrodes were 1.25 mm wide and spaced 2.5 mm apart. The pacing current was 10 mA with a pulse width of 2 ms.

Figure 3C shows the array positioned over the left anterior descending (LAD) coronary artery (yellow arrows), with the pacing

catheter (white arrow) positioned just inferior to the array. The presence of the epicardial coronary artery did not cause any noticeable distortion to the recording. As predicted previously, the adhesion energy between the wet surface and the electrode array was sufficient to hold the array onto the surface of the heart. If the pericardium were intact, as it would be during a catheter-based procedure, the electrode would be bathed in fluid and the forces would be quite different. In this case, we anticipate that tension of the

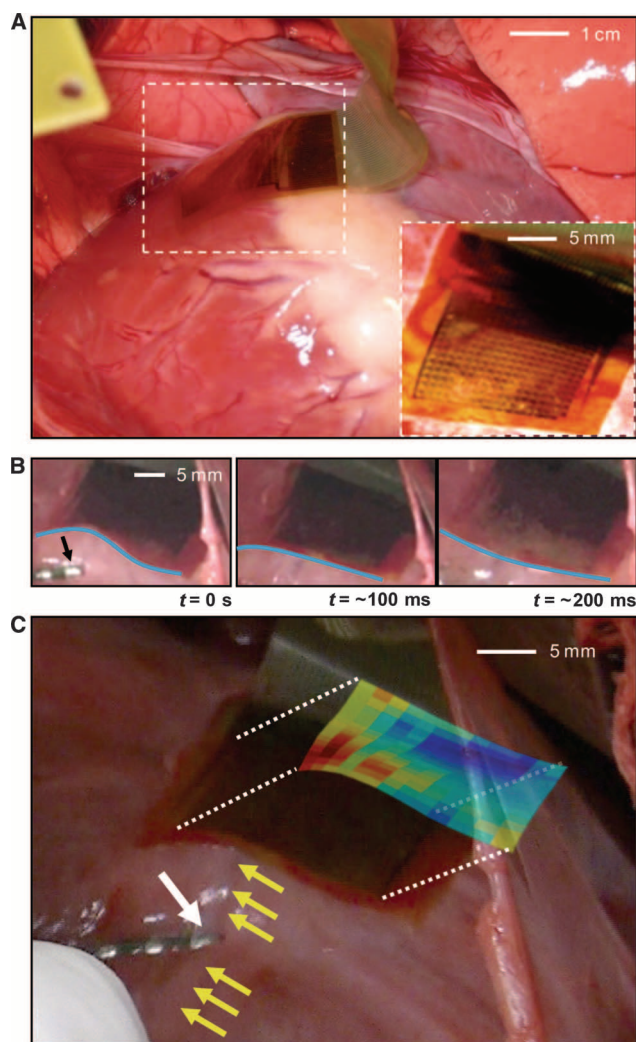


**Fig. 3.** Photographs of a flexible electrophysiology mapping device on the porcine heart. **(A)** Photograph of flexible device conforming to the cardiac tissue via surface tension. (Inset) Magnified image at a different viewing angle. **(B)** Sequence of movie frames collected at different times during the contraction cycle of the heart, illustrating the ability of the device to bend in a way that maintains intimate, conformal contact with the tissue during cardiac rhythm. Blue lines highlight the degree of bending along the device. A conventional pacing electrode is indicated in the left-most frame (black arrow). **(C)** Photograph of a device on the LAD coronary artery (yellow arrows), with overlaid color map of the relative time of depolarization from paced activation. The white arrow in the lower left indicates the pacing electrode, and the red colors in the activation map indicate the areas of earliest response.

space between the epicardium and the pericardium will hold the array in contact. The color-coded map in Fig. 3C shows a visual representation of the data collected from the device, with the procedures described below.

Data from all channels were filtered and processed with custom MATLAB software to determine the relative activation time at each contact by comparing the time of the maximum negative slope ( $dV/dt$ ) of the unipolar electrogram to the maximum negative slope of the average electrogram of all 288 channels. These activation times were then used to generate isochronal maps showing propagation of paced and unpaced cardiac depolarization wavefronts spreading across the array for a variety of recording sites and pacing conditions (movie M2 and fig. S24). Sample voltage trace data from a single channel without remote pacing are shown in Fig. 4A. The noise level of the recording was very low (Fig. 4A, inset), with an SNR of  $\sim 34$  dB. Voltage data for all channels taken at four points in time and plotted as a color image show a wave of cardiac activation moving from the left side of the array to the right side (Fig. 4B). Dashed lines plotted

on an average voltage trace collected from all of the electrodes illustrate the instant in time that each frame in Fig. 4B was taken (Fig. 4C). A similar plot of externally paced data shows a wave of cardiac activation moving from the right side of the array to the left side (fig. S16). Figure S24 and movie M2 detail all of the voltage data presented in Fig. 4B. The response of the electrodes was uniform, as we determined by plotting the average peak amplitude of the cardiac activation (fig. S14).

We used the voltage data to develop an isochronal activation map, illustrating the natural activation pattern of the heart (Fig. 4E). Data from 3 of the 18 columns were removed due to failures in the metal interconnections, related to imperfections in the fabrication. Conduction velocities could be computed even with defective columns by linear interpolation by using knowledge of the spatial locations of the remaining columns. All of the remaining channels and all rows functioned properly.

We also collected data with remote pacing and generated isochronal maps by pacing from three different locations relative to the

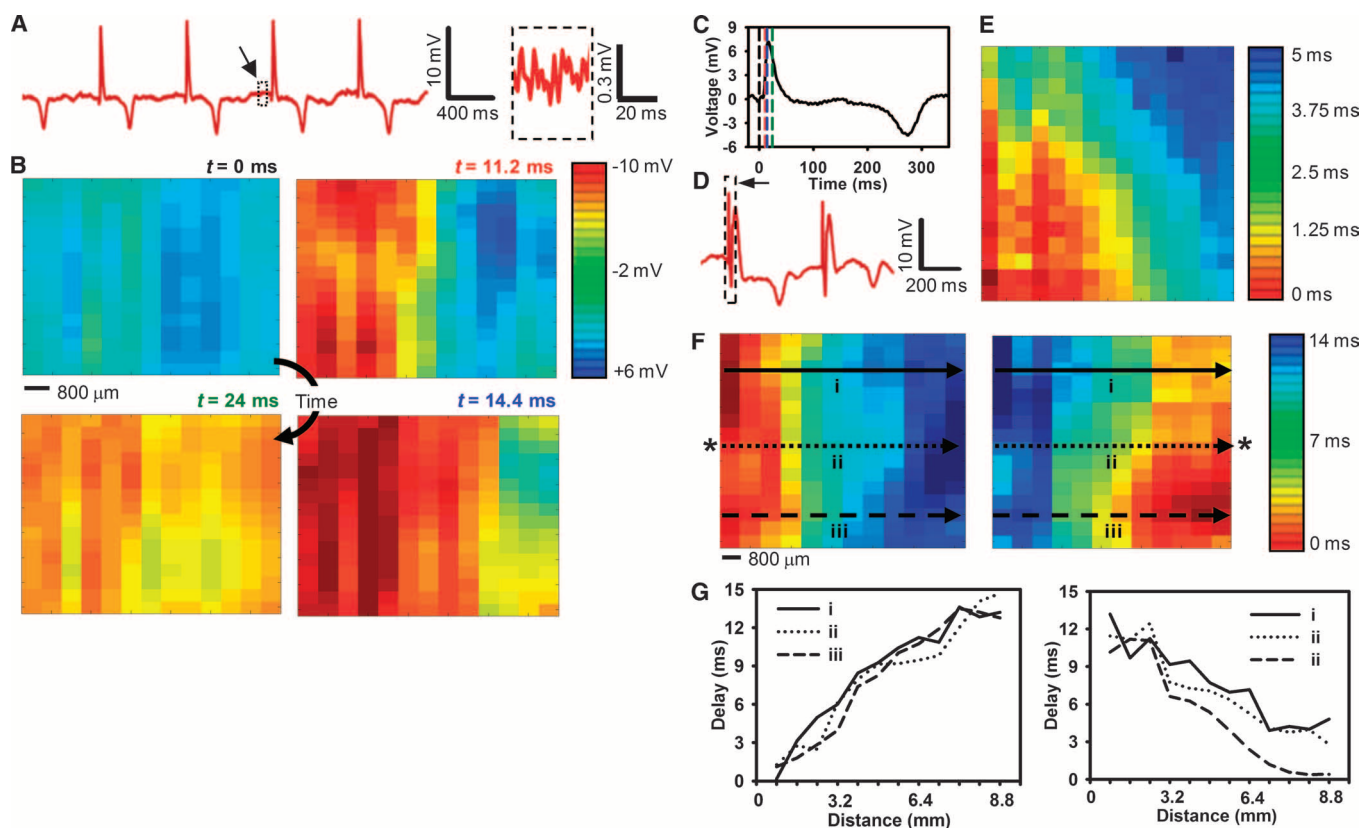


**Fig. 4.** Representative data recorded from the epicardial surface of the porcine heart with a flexible electrophysiology mapping device. **(A)** Representative single voltage trace without external pacing. (Inset) A magnified view of the system noise. Black arrow, source of the inset data. The SNR of the recorded signal was  $\sim 34$  dB. **(B)** Representative voltage data for all electrodes at four points in time showing normal cardiac wavefront propagation. Voltage is plotted with the color scale in the right corner. **(C)** Average voltage from all electrodes illustrating the point in time that each frame in (B) was taken (dotted line). The color of the dashed lines corresponds to the color of the time label in (B). **(D)** Representative single voltage trace with external pacing from a standard clinical electrode. The

black arrow and dotted line box highlight the pacing artifact. Note that negative is plotted up by convention in (A), (C), and (D). **(E)** Isochronal activation map with pacing. **(F)** Color map of relative activation times for two different external pacing sites. The activation times are plotted with the color scale shown at the right. Asterisks (\*) indicate the relative location of the external pacing electrode. The scale bar illustrates the spacing between electrode locations. **(G)** The data from the activation map at the locations marked by lines i to iii are plotted. Activation delay plotted as a function of distance from the left side of the array for selected rows indicated by the arrows in (F). Data from five columns in (B) and six columns in (E) were removed due to failures in the metal interconnections.

array (Fig. 4F and fig. S15). A sample of the raw voltage data from a single channel is shown to illustrate the typical waveforms (Fig. 4D). The complete data used to generate the isochronal map in the left and right panels of Fig. 4F are provided in figs. S25 and S26 and movies M3 and M4, respectively.

On the basis of the relative activation times, conduction velocity across the array (transverse to fiber axis) was 0.9 mm/ms (Fig. 4F); the velocity in the longitudinal direction (approximately parallel to the orientation of the LAD coronary artery) was faster by a factor of 3 (fig. S15). These results are consistent with anisotropic conduction properties measured in previous studies using mammalian hearts (19, 20).

Plots of the delay to activation as a function of distance across the device for selected rows of the electrode array along the arrows in Fig. 4F further illustrate the linear wavefront propagation recorded by the device (Fig. 4G).

## DISCUSSION

The conformal, bio-interfaced electronic systems described here represent an example of a new class of cardiac electrophysiological devices that can map entire regions of the epicardial surface at high speed without the need for manual repositioning or manual operation. This device combines high-performance transistors in circuits with medium-scale levels of integration (~2000 transistors) to form electrodes on a plastic substrate and has the following characteristics: (i) local current amplification by means of an amplifier at each electrode, to enable accurate measurements of the small, ~1 mV, electrical potentials associated with cardiac conduction; (ii) transistor switching speeds approaching 1 MHz, to enable multiplexed sampling of fast biological signals of millisecond duration; (iii) multiplexed sampling to combine signals from high-density arrays of sensors (288 independent channels) into a minimal number of external connections (36 wires); (iv) water-proof design for reliable operation when completely submerged in biological fluids for extended periods (hours); (v) low bending stiffness that enables adhesion to the constantly moving epicardial surface by physical lamination, without adhesives or penetrating pins; and (vi) neutral mechanical plane layouts that locate the silicon nanoribbons at the middle of the device so that they are not subjected to mechanical strain, thereby eliminating any measurable variation in the system behavior with bending.

A number of improvements are possible that would enhance the device presented above. For clinical applications, platinum or platinum-iridium should be used for the electrode contact instead of gold because it lowers the output impedance of the electrode and enhances signal quality. Increasing the number of functioning channels by a significant amount, in a manner that retains high yields after fabrication and handling, requires further optimization of processing conditions and might demand the use of cleanroom facilities configured for manufacturing rather than academic research. Such commercial facilities offer appropriate levels of control and automation for large increases in yield relative to that possible with manual processing in research environments. Finally, although the system noise of the present configuration is acceptable for cardiac applications, it could be reduced further through the use of complementary circuits to provide voltage gain and analog to digital converters with lower noise.

In addition to advances in performance, additional functions could be developed for this device. For example, with straightforward additions to the circuits and external control, the same systems could provide multisite cardiac pacing with closed-loop feedback of local ventricular contractility or cardiac output measurements via distributed arrays of stimulation electrodes and corresponding active circuits for them. Furthermore, the mechanical properties of the flexible circuits permit their packaging in catheter-based delivery systems. The circuit itself can be rolled up and inserted into a catheter for non-surgical delivery to cardiac or other sites within the body. This same flexibility confers on the device the ability to deploy on and conform to large and small, irregular curvilinear surfaces in the body, such as the brain or peripheral nervous system.

More generally, the results presented here could provide the basis for clinically useful, implantable devices that overcome limitations associated with the long-standing requirement of one wire for each sensor through the use of active electronics formed on flexible sheets of plastic. The capacity to intimately integrate modern semiconductor technology with the soft, fluid-bathed, curvilinear and moving surfaces of the human body may enable the development of advanced devices for diagnostic, therapeutic, and surgical applications.

## MATERIALS AND METHODS

### Circuit design

Each unit cell incorporates an nMOS-based source-follower amplifier configuration. This circuit provides significant current gain to enable fast switching of the multiplexers by supplying the current needed to charge the parasitic output capacitances. These unintended additional capacitances come from several sources, including the inactive multiplexing transistors in a given column, the ~2-foot-long cables that connect the electrode array to the interface circuit board, the circuit board itself, and the input capacitance of its buffer amplifiers.

Power is supplied to the array via the +V and -V connections. Split power supplies are used to allow the physiologic signals biased around 0 V to remain well within the linear input range of the amplifiers. The linear input range is approximately  $(-V + V_t)$  to +V, where  $V_t$  is the transistor threshold voltage (~0.7 V). A conventional reference electrode, ground pad, or bone screw is connected through a current meter to the power supply and acquisition system ground terminal. This biases the recorded signals around 0 V.

The absolute maximum input range for the device is determined by the gate to source breakdown voltage, likely at least  $\pm 20$  V. Further protection from transients, such as those caused by cardiac defibrillation, can be added with standard electrostatic discharge protection techniques.

The device is expected to remain fully operational when exposed to  $\gamma$  radiation during fluoroscopic procedures because the level of radiation exposure is orders of magnitude lower than levels known to cause performance changes in silicon transistor circuits of this size (21). Further testing is needed to qualify the performance of this device while exposed to radiation.

### Circuit fabrication

The fabrication starts with the preparation of the PI substrate (25  $\mu$ m) (Kapton). For ease of handling, a sheet of this material was attached to a glass slide coated with a thin layer of poly(dimethylsiloxane)

(PDMS) as a soft adhesive. Separately doped silicon nanoribbons were prepared through a high-temperature diffusion process using a p-type silicon-on-insulator (SOI) wafer [Si(260 nm)/SiO<sub>2</sub>(1000 nm)/Si] (Soitec) and phosphorus spin-on-dopant (SOD) (P509) (Filmtronics). A 300-nm-thick layer of SiO<sub>2</sub> deposited by plasma-enhanced chemical vapor deposition (PECVD) served as the diffusion barrier mask. Doping regions were defined through conventional photolithography and CF<sub>4</sub>/O<sub>2</sub> reactive ion etching (RIE). The diffusion was performed at 950° to 1000°C in a rapid thermal annealing system. A series of wet etching steps with hydrofluoric acid and piranha solution (H<sub>2</sub>O<sub>2</sub> and H<sub>2</sub>SO<sub>4</sub> mixture) removed the SOD and SiO<sub>2</sub>.

Doped nanomembranes derived by patterned etching of the top silicon layer of the SOI wafer were transfer-printed onto the PI substrate with a thin, spin-cast layer of a precursor to PI as an adhesive. To prepare the structures for transfer, we etched away the buried SiO<sub>2</sub> layer with concentrated HF solution to yield freestanding nanomembranes. The PI precursor was cured at 300°C for 1 hour immediately after printing. Further isolation of the active Si components, such as source, drain, and channel regions, was accomplished by photolithography and RIE with SF<sub>6</sub>. A thin gate oxide of SiO<sub>2</sub> (~100 nm) was then deposited by PECVD. The source or drain contact regions were opened with buffered oxide etchant through a photolithographically patterned mask. The gate electrodes and metal interconnects were deposited by electron evaporation of Cr/Au (~5 nm/~145 nm) and patterned through wet etching. Each unit cell contains seven transistors, interconnected by wiring as described in the main text. Isolation of the metal layers was accomplished with a PI interlayer dielectric with thickness of 1.4 μm. Connections between layers were established through holes defined by patterned RIE with O<sub>2</sub>. A stack of organic or inorganic insulation layers followed by encapsulation with a photocurable epoxy (SU8) (Microchem) formed a water-tight seal. After insulation, we used the flexible heat seal connector to connect the electrodes with the DAQ system through an adapter circuit board. The design of this adapter board is shown in fig. S17. Detailed insulation and heat seal connection processes are described below.

### Barriers to biological fluids

Because the measurement environment is wet and contains a large number of ions from the saline solution, a multilayer barrier strategy is used to prevent leakage currents that would be dangerous for the animal. An inorganic or organic multilayer and an additional thick organic insulation layer were used for this purpose (figs. S3 and S4). After spin coating the PI interlayer dielectric and subsequent dry etching to create vias, the first metal layers are connected to the second metal layer (yellow) through the first via (purple), which completes the device fabrication process (fig. S4). In the encapsulation design, we used a staggered via structure, between via 2 and via 3. By intentional misalignment of the vias, the first via can be completely covered by the final epoxy layer. Figure S5 shows the final microscope image after the insulation.

### Interconnection scheme

After device fabrication, the flexible sensor is interconnected to the circuit board through a flexible ACF film. For this connection, heat and pressure are applied. After alignment between ACF film and the sample, clipping with conventional metal clips provides enough pressure for the connection. A piece of PDMS and glass can be added to prevent mechanical failure in samples during clipping and to spread pressure

over the whole connection area (fig. S6A). After clipping, heating at 180°C for 15 min results in a mechanically and electrically sound connection between the metal and the ACF film (fig. S6, B and C).

### Acquisition system

The adapter circuit board was connected via a standard 40-pin ribbon cable to the main interface circuit board (figs. S18 to S21). This custom circuit board provided the row select signals to the electrode array and provided buffering of the analog output signals from the array. The buffering was accomplished by TLC2274 Op Amps (Texas Instruments). This stage of buffering further reduced the output impedance to allow for longer cable runs and improved switching speed. The outputs of this circuit board were connected to National Instruments PXI-6281 and USB-6259 high-speed M series multifunction DAQ modules via standard BNC cables. The DAQ modules were used to generate the row select signals and to sample the multiplexed analog output signals from the electrode array. In total, 18 analog input channels were used. Data were acquired, demultiplexed, stored, and displayed with custom MATLAB software (The MathWorks).

### Circuit simulation

Simulations were performed with the spectreS simulator (Cadence) (figs. S22 and S23). The NCSU\_TechLib\_ami06 tech library was used for all of the transistors.

### Data processing

Data from all channels were high-pass filtered at 1 Hz and up-sampled by a factor of 20 to a sampling rate of 12.5 kHz before processing. Up-sampling allowed the relative activation times to be computed with subsample time accuracy because data from multiple heart beats were averaged. After up-sampling, the data were smoothed and demeaned to remove the DC bias. An average signal was constructed, and the derivative was taken to identify the relative activation times by using an automatic peak search algorithm.

### Circuit mechanics

For a thin film of length  $L$  and bending stiffness  $B$  wrapping on a cylinder of radius  $R$  (fig. S9A), the total energy of the wrapped state is composed of two parts: the bending energy in the thin film  $U_b$  and the adhesion energy  $U_a$  between the thin film and the cylinder. The bending energy in the thin film is

$$\frac{1}{2}U_b = \frac{1}{2}B\kappa^2L = \frac{B}{2R^2}L \quad (1)$$

The adhesion energy is

$$\frac{1}{2}U_a = -\gamma L \quad (2)$$

where  $\gamma$  is the adhesion energy (per unit area) between the thin film and the cylinder. If  $U_b + U_a < 0$  (the unwrapped state has energy of 0), the wrapped state is energetically favorable, and thus, the thin film wraps around the cylinder. This gives

$$\gamma > \frac{B}{2R^2} \quad (3)$$

The cross-sectional layout of the circuit, which will be used to determine the bending stiffness  $B$ , is shown in fig. S9B. The top SU8

layer has a thickness  $h_1 = 18 \mu\text{m}$ , Young's modulus  $E_{\text{SU8}} = 5.6 \text{ GPa}$ , and Poisson's ratio  $\nu_{\text{SU8}} = 0.22$  (22). The bottom PI layer has a thickness  $h_2 = 25 \mu\text{m}$ , Young's modulus  $E_{\text{PI}} = 3.4 \text{ GPa}$ , and Poisson's ratio  $\nu_{\text{PI}} = 0.34$  (23). The middle layer, of thickness  $\sim 5 \mu\text{m}$ , is composed of several different components. The material and thickness of each component are shown in fig. S9B, and their Young's moduli are  $E_{\text{Si}} = 150 \text{ GPa}$ ,  $E_{\text{SiO}_2} = 72 \text{ GPa}$ ,  $E_{\text{Au}} = 78 \text{ GPa}$ ,  $E_{\text{Si}_3\text{N}_4} = 194 \text{ GPa}$ . Because each of these components only occupies a small portion of each layer of material, the position of the mechanical neutral axis can be approximately obtained as (within a few percent error)

$$y_0 = \frac{1}{2} \frac{\bar{E}_{\text{PI}} h_2^2 + \bar{E}_{\text{SU8}} h_1 (2h_2 + h_1)}{\bar{E}_{\text{PI}} h_2 + \bar{E}_{\text{SU8}} h_1} \quad (4)$$

where  $\bar{E}_{\text{PI}} = E_{\text{PI}} / (1 - \nu_{\text{PI}}^2)$  and  $\bar{E}_{\text{SU8}} = E_{\text{SU8}} / (1 - \nu_{\text{SU8}}^2)$  are the plain strain moduli of PI and SU8, respectively. The bending stiffness of the circuit is

$$B = \bar{E}_{\text{PI}} h_2 \left( \frac{1}{3} h_2^2 - h_2 y_0 + y_0^2 \right) + \bar{E}_{\text{SU8}} h_1 \left[ \frac{1}{3} h_1^2 + h_1 (h_2 - y_0) + (h_2 - y_0)^2 \right] \quad (5)$$

The strain at a point of coordinate  $y$  is given by

$$\varepsilon = \frac{y - y_0}{R_b} \quad (6)$$

where  $R_b$  is the bending radius of curvature of the circuit. The position of the mechanical neutral axis is calculated as  $y_0 = 26.5 \mu\text{m}$ . With the bending stiffness given by Eq. 5, Eq. 3 gives  $\gamma > 8.7 \text{ mJ/m}^2$ . For a bending radius  $R_b = 5 \text{ cm}$ , the maximum strain in Si and SiO<sub>2</sub> is  $\sim 0.001\%$  and  $\sim 0.0001\%$ , respectively; the strains in the four Au layers are  $\sim 0.001$ ,  $0.004$ ,  $0.03$ , and  $0.05\%$ , respectively.

### Animal experiments

The array was placed on the heart of an adult pig and conformed to the epicardial surface, including epicardial coronary vessels (Fig. 3). Initially, the array was positioned between the epicardium and the parietal pericardium, where it was demonstrated to slide easily across the surface of the heart. This behavior was not desirable for the current experiment because it changes the position of the device on the heart in an uncontrolled manner. Subsequently, the parietal pericardium was removed, and the array was left to stay in position via surface tension alone. We anticipate that in a clinical situation in which the device is introduced by a percutaneous catheter, the device would stay in place on the cardiac surface through the additional anchoring force provided by the catheter, the pericardium, and the other surrounding tissues. These aspects must be verified through in vivo testing.

The heart was externally paced via a standard, nonsteerable decapolar electrode electrophysiology catheter (Boston Scientific) held in contact with the epicardial surface.

### SUPPLEMENTARY MATERIAL

www.sciencetranslationalmedicine.org/cgi/content/full/2/24/24ra22/DC1

Fig. S1. Schematic illustration corresponding to steps for fabricating active, conformal electronics for cardiac electrophysiology mapping.

Fig. S2. Magnified view of a completed device in a slightly bent state to illustrate detail.

Fig. S3. Physical layout of a single unit cell.

Fig. S4. Sequential process of trilayer organic or inorganic stack fabrication.

Fig. S5. Optical microscope image of a single unit cell with completed insulation layers.

Fig. S6. ACF connection process.

Fig. S7. Simplified schematic diagram of a source-follower buffer amplifier, as used in the basic unit cell design.

Fig. S8. Image of acquisition system during the animal experiment.

Fig. S9. SNR dependence on multiplexing frequency for a 20-Hz test signal.

Fig. S10. Calculated induced strain in each layer of the device during tight folding.

Fig. S11. Schematic diagram of wrapping model and cross-sectional view of sensor.

Fig. S12. Sine wave response (at 5 Hz) before and after saline immersion for 3 hours.

Fig. S13. Images of experiment with porcine animal model.

Fig. S14. Color map illustrating the amplitude uniformity of all of the channels.

Fig. S15. Isochronal activation map with pacing.

Fig. S16. Representative voltage data for all electrodes at four points in time showing paced cardiac wavefront propagation.

Fig. S17. Design of the adapter circuit board, which adapts the ACF ribbon to a 40-pin connector.

Figs. S18 to S21. Schematic design and layout of the main interface circuit board, which connects the 40-pin ribbon cable to the acquisition system.

Fig. S22. Screenshot from Cadence simulation environment showing the schematic of one unit cell of the array.

Fig. S23. Screenshot from Cadence simulation environment showing the test setup for two unit cells connected to a common output.

Fig. S24. Four seconds of raw data corresponding to movie M2.

Fig. S25. Two seconds of raw data corresponding to movie M3.

Fig. S26. Two seconds of raw data corresponding to movie M4.

Movie M1. Animal experiment.

Movie M2. Unpaced voltage data from all electrodes illustrating the natural activation pattern of the heart.

Movie M3. Voltage data from all electrodes illustrating the paced activation pattern of the heart moving from the left side of the array to the right side.

Movie M4. Voltage data from all electrodes illustrating the paced activation pattern of the heart moving from the right side of the array to the left side.

### REFERENCES AND NOTES

1. E. M. Aliot, W. G. Stevenson, J. M. Almendral-Garrote, F. Bogun, C. H. Calkins, E. Delacretaz, P. D. Bella, G. Hindricks, P. Jais, M. E. Josephson, J. Kautzner, G. N. Kay, K. H. Kuck, B. B. Lerman, F. Marchlinski, V. Reddy, M. J. Schaliq, R. Schilling, K. Soejima, D. Wilber; European Heart Rhythm Association; European Society of Cardiology; Heart Rhythm Society, EHRA/HRS Expert Consensus on Catheter Ablation of Ventricular Arrhythmias: Developed in a partnership with the European Heart Rhythm Association (EHRA), a Registered Branch of the European Society of Cardiology (ESC), and the Heart Rhythm Society (HRS); in collaboration with the American College of Cardiology (ACC) and the American Heart Association (AHA). *Europace* **11**, 771–817 (2009).
2. B. J. Scherlag, S. H. Lau, R. H. Helfant, W. D. Berkowitz, E. Stein, A. N. Damato, Catheter technique for recording His bundle activity in man. *Circulation* **39**, 13–18 (1969).
3. G. H. Gelinck, H. E. Huitema, E. van Veenendaal, E. Cantatore, L. Schrijnemakers, J. B. van der Putten, T. C. Geuns, M. Beenhakkers, J. B. Giesbers, B. H. Huisman, E. J. Meijer, E. M. Benito, F. J. Touwslager, A. W. Marsman, B. J. van Rens, D. M. de Leeuw, Flexible active-matrix displays and shift registers based on solution-processed organic transistors. *Nat. Mater.* **3**, 106–110 (2004).
4. E. Cantatore, T. C. T. Geuns, G. H. Gelinck, E. van Veenendaal, A. F. A. Gruijthuisen, L. Schrijnemakers, S. Drews, D. M. de Leeuw, A 13.56-MHz RFID system based on organic transponders. *IEEE J. Solid-St. Circ.* **42**, 84–92 (2006).
5. A. J. Baca, J. H. Ahn, Y. Sun, M. A. Meitl, E. Menard, H. S. Kim, W. M. Choi, D. H. Kim, Y. Huang, J. A. Rogers, Semiconductor wires and ribbons for high-performance flexible electronics. *Angew. Chem. Int. Ed. Engl.* **47**, 5524–5542 (2008).
6. D. Y. Khang, H. Jiang, Y. Huang, J. A. Rogers, A stretchable form of single-crystal silicon for high-performance electronics on rubber substrates. *Science* **311**, 208–212 (2006).
7. D. H. Kim, J. H. Ahn, W. M. Choi, H. S. Kim, T. H. Kim, J. Song, Y. Y. Huang, Z. Liu, C. Lu, J. A. Rogers, Stretchable and foldable silicon integrated circuits. *Science* **320**, 507–511 (2008).
8. T. Sekitani, Y. Noguchi, K. Hata, T. Fukushima, T. Aida, T. Someya, A rubberlike stretchable active matrix using elastic conductors. *Science* **321**, 1468–1472 (2008).
9. D.-H. Kim, J. A. Rogers, Stretchable electronics: Materials strategies and devices. *Adv. Mater.* **20**, 4887–4892 (2008).
10. H. C. Ko, M. P. Stoykovich, J. Song, V. Malyarchuk, W. M. Choi, C. J. Yu, J. B. Geddes III, J. Xiao, S. Wang, Y. Huang, J. A. Rogers, A hemispherical electronic eye camera based on compressible silicon optoelectronics. *Nature* **454**, 748–753 (2008).

11. D. H. Kim, J. Song, W. M. Choi, H. S. Kim, R. H. Kim, Z. Liu, Y. Y. Huang, K. C. Hwang, Y. W. Zhang, J. A. Rogers, Materials and noncoplanar mesh designs for integrated circuits with linear elastic responses to extreme mechanical deformations. *Proc. Natl. Acad. Sci. U.S.A.* **105**, 18675–18680 (2008).
12. F. Patolsky, B. P. Timko, G. Yu, Y. Fang, A. B. Greytak, G. Zheng, C. M. Lieber, Detection, stimulation, and inhibition of neuronal signals with high-density nanowire transistor arrays. *Science* **313**, 1100–1104 (2006).
13. B. P. Timko, T. Cohen-Karni, G. Yu, Q. Qing, B. Tian, C. M. Lieber, Electrical recording from hearts with flexible nanowire device arrays. *Nano Lett.* **9**, 914–918 (2009).
14. B. G. Streetman, S. K. Banerjee, in *Solid State Electronic Devices* (Pearson, New Jersey, ed. 6, 1981).
15. S. E. Thompson, M. Armstrong, C. Auth, M. Alavi, M. Buehler, R. Chau, S. Cea, T. Ghani, G. Glass, T. Hoffman, C.-H. Jan, C. Kenyon, J. Klaus, K. Kuhn, Z. Ma, B. McIntyre, K. Mistry, A. Murthy, B. Obradovic, R. Nagisetty, P. Nguyen, S. Sivakumar, R. Shaheed, L. Shifren, B. Tufts, S. Tyagi, M. Bohr, Y. El-Mansy, A 90-nm logic technology featuring strained-silicon. *IEEE Trans. Electron Devices* **51**, 1790–1797 (2004).
16. M. K. Chaudhury, G. M. Whitesides, Direct measurement of interfacial interactions between semispherical lenses and flat sheets of poly(dimethylsiloxane) and their chemical derivatives. *Langmuir* **7**, 1013–1025 (1991).
17. J. Qian, H. Gao, Scaling effects of wet adhesion in biological attachment systems. *Acta Biomater.* **2**, 51–58 (2006).
18. T. A. Michalske, E. R. Fuller Jr., Closure and repropagation of healed cracks in silicate glass. *J. Am. Ceram. Soc.* **68**, 586–590 (2006).
19. A. Kadish, M. Shinnar, E. N. Moore, J. H. Levine, C. W. Balke, J. F. Spear, Interaction of fiber orientation and direction of impulse propagation with anatomic barriers in anisotropic canine myocardium. *Circulation* **78**, 1478–1494 (1988).
20. L. Clerc, Directional differences of impulse spread in trabecular muscle from mammalian heart. *J. Physiol.* **255**, 335–346 (1976).
21. P. L. Medhurst, D. J. Foster, Effects of  $\gamma$  radiation on threshold voltages of trench isolated CMOS. *Electron. Lett.* **25**, 1155–1156 (1989).
22. A. T. Al-Halhouli, I. Kampen, T. Krahl, S. Buttgenbach, Nanoindentation testing of SU-8 photoresist mechanical properties. *Microelectron. Eng.* **85**, 942–944 (2008).
23. D. Y. W. Yu, F. Spaepen, The yield strength of thin copper films on Kapton. *J. Appl. Phys.* **95**, 2991–2997 (2004).
24. **Acknowledgments:** We thank T. Banks and J. A. N. T. Soares for help in using facilities at the Frederick Seitz Materials Research Laboratory, and C. Wilkinson for coordinating collaborative experiments at the University of Pennsylvania. **Funding:** This work was supported by a National Security Science and Engineering Faculty Fellowship and the U.S. Department of Energy, Division of Materials Sciences under Award no. DEFG02-91ER45439, through the Frederick Seitz Materials Research Laboratory and Center for Microanalysis of Materials at the University of Illinois at Urbana-Champaign. Work at the University of Pennsylvania is supported by NIH grants NINDS R01-NS041811-04 and R01 NS 48598-04, the Klingenstein Foundation, and The Epilepsy Therapy Project. **Author contributions:** J.V., D.-H.K., J.D.M., Y.-S.K., N.A., D.J.C., J.X., Y.H., J.A.R., and B.L. designed the experiments. J.V., D.-H.K., J.D.M., Y.-S.K., D.J.C., J.X., and Y.H. performed the experiments and analysis. J.V., D.-H.K., J.D.M., D.J.C., J.A.B., J.A.R., and B.L. wrote the paper. **Competing interests:** J.A.B., D.J.C., B.L., J.A.R., and J.V. hold patents on this technology, “Flexible and Scalable Sensor Arrays for Recording and Modulating Physiologic Activity” and “A novel, flexible, high-density, active electrode array for advanced cardiac resynchronization therapy.” The Universities of Pennsylvania and Illinois have licensed this technology to MC10, a company interested in general systems of the type described in this manuscript. J.A.R. is a founder of and sits on the Board of Directors of MC10. B.L. is a consultant for MC10.

Submitted 15 December 2009

Accepted 12 March 2010

Published 24 March 2010

10.1126/scitranslmed.3000738

**Citation:** J. Viventi, D.-H. Kim, J. D. Moss, Y.-S. Kim, J. A. Blanco, N. Annetta, A. Hicks, J. Xiao, Y. Huang, D. J. Callans, J. A. Rogers, B. Litt, A conformal, bio-interfaced class of silicon electronics for mapping cardiac electrophysiology. *Sci. Transl. Med.* **2**, 24ra22 (2010).